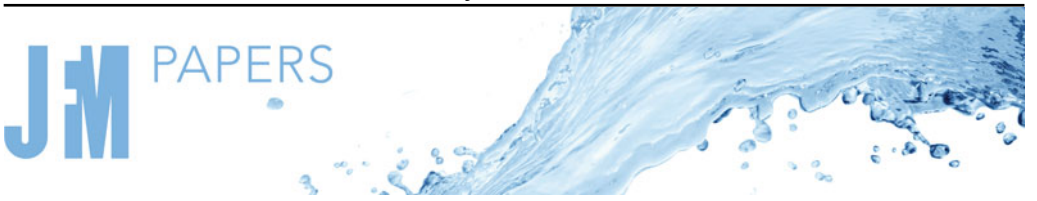
J. Fluid Mech. (2025), *vol.* 1021, A32, doi:10.1017/jfm.2025.10719



Dynamical properties of ocean internal solitary waves: a study based on the modified intermediate long wave equation

Di Yu[1] **and Jinbao Song**[1]

[1]State Key Laboratory of Ocean Sensing & Ocean College, Zhejiang University, Zhoushan 316021, PR China

Corresponding author: Jinbao Song, songjb@zju.edu.cn

(Received 26 February 2025; revised 11 September 2025; accepted 14 September 2025)

This study presents a modified intermediate long wave (mILW) equation derived from the Navier–Stokes equations via multi-scale analysis and perturbation expansion, aimed at describing internal solitary waves (ISWs) in finite-depth, stratified oceans. Compared to the classical ILW model, the proposed mILW equation incorporates cubic nonlinearities and captures the dynamical behaviour of large-amplitude ISWs more accurately. The equation reduces to the modified Korteweg–de Vries equation and modified Benjamin–Ono equations in the shallow- and deep-water limits, respectively, thus providing a unified framework across varying depth regimes. Soliton solutions are constructed analytically using Hirota's bilinear method, and numerical simulations investigate wave–wave interactions, including rogue waves and Mach reflection. Furthermore, a smooth tanh-type density profile is adopted to reflect realistic stratification. Associated vertical modal structures and vertical velocity fields are analysed, and higher-order statistics (skewness and kurtosis) are introduced to reveal the density dependence of wave asymmetry. The results offer new insights into the nonlinear dynamics of ISWs, with implications for ocean mixing, energy transport and submarine acoustics.

Key words: internal waves, Navier-Stokes equations, solitary waves

1. Introduction

Internal solitary waves (ISWs), a specific type of nonlinear internal wave, are ubiquitous in stratified fluids such as oceans and lakes. These waves arise due to density stratification and exhibit a localised, solitary nature, maintaining their shape and speed over long distances without significant dispersion (Helfrich & Melville 2006). They play a critical role in oceanographic processes, influencing mixing, energy transport, sediment resuspension, and even marine ecosystem dynamics (Jia *et al.* 2019; Li 2023; Ren *et al.* 2023). Over

© The Author(s), 2025. Published by Cambridge University Press.

https://doi.org/10.1017/jfm.2025.10719 Published online by Cambridge University Press

recent decades, ISWs have attracted substantial attention due to their implications in ocean engineering, marine ecosystems and military applications (Guo & Chen 2014; Zeidan, Pandey & Govekar 2022). Observations from field studies and remote sensing have revealed their presence in diverse marine environments, from continental shelves to deep ocean basins (Klemas & Yan 2014). Given their importance, understanding the generation, propagation and interaction of ISWs is fundamental to both physical oceanography and applied sciences such as underwater communication and military operations (Adem & Khalique 2013; Xu *et al.* 2016).

A wide range of theoretical models has been developed to describe the propagation of ISWs; classical theories for ISWs are rooted in weakly nonlinear models such as the Korteweg–de Vries (KdV) equation (Korteweg & de Vries 1895) for shallow water, and the Benjamin–Ono (BO) equation (Benjamin 1966; Ono 1975) for deep water. The classical KdV framework balances quadratic nonlinearity uu_x and third-order dispersion u_{xxx}. It effectively explains ISW stability and soliton interactions (Benjamin 1966). For deep-water regimes, the BO equation extends this paradigm, incorporating non-local dispersion to model waves in infinitely stratified fluids (Ono 1975). However, these models are inherently limited to asymptotic depth extremes – shallow or deep water – and fail to capture the dynamics of finite-depth oceanic environments, where neither approximation holds.

A critical limitation of the KdV and BO frameworks lies in their treatment of nonlinearity. While they accurately describe small-amplitude waves, their weakly nonlinear assumptions break down for large-amplitude ISWs, which exhibit stronger nonlinear steepening and higher-order dispersion effects. For instance, field observations and laboratory experiments have revealed discrepancies in wave amplitude decay rates and interaction patterns when compared to KdV predictions, particularly in transitional depth regions (Lamb & Xiao 1996; Cai, Long & Gan 2019). To address this limitation, various modified equations have been proposed, incorporating stronger nonlinear effects and enabling the study of ISWs with larger amplitudes and steeper gradients (Vishnu Priya, Thulasidharan & Senthilvelan 2025). Modified formulations such as the modified KdV (mKdV) equation,

$$u_t + 6u^2u_x + u_{xxx} = 0, \tag{1.1}$$

and the extended KdV (eKdV) equation, incorporating higher-order nonlinear and dispersive terms, have been proposed. Ren *et al.* (2023) derived an extremely complex higher-order BO equation, including multiple high-order nonlinear and non-local terms. These models better capture strong nonlinearity and wave–wave interactions, but remain confined to specific depth regimes, lacking a unified framework for finite-depth oceans.

In the finite-depth regime, where both nonlinear and dispersive effects are significant, the intermediate long wave (ILW) equation (Joseph 1977; Kubota, Ko & Dobbs 1978) provides a suitable theoretical framework. Among the various mathematical models developed to describe ISWs, the ILW equation serves as a cornerstone for finite-depth fluids, bridging the shallow-water KdV equation and the deep-water BO equation (Joseph 1977; Cullen & Ivanov 2020). While the ILW equation successfully captures many features of ISWs, it assumes relatively weak nonlinearity and small amplitudes, still has limitations in dealing with higher-order nonlinearity, and limits its applicability to large-amplitude wave scenarios commonly observed in nature (Li 2024; Zhi, Fan & You 2024). Classical ILW theory neglects higher-order nonlinearities, restricting its applicability to moderate-amplitude waves (Kubota *et al.* 1978). Recent advances in computational fluid dynamics and field measurements have further exposed these shortcomings, particularly in scenarios involving stronger nonlinear effects, complex soliton dynamics, or interactions with complex topography (Vlasenko & Stashchuk 2015; Fedele *et al.* 2016; McAllister

https://doi.org/10.1017/jfm.2025.10719 Published online by Cambridge University Press

et al. 2024). Such gaps underscore the need for generalised theoretical frameworks that unify shallow- and deep-water limits while accommodating stronger nonlinear effects.

In this study, we derive a modified ILW (mILW) equation that extends the theoretical framework to accommodate stronger nonlinearities and larger amplitudes. The main contents of this paper are as follows. First, by integrating the nonlinear theory, perturbation expansion and multi-scale analysis, an mILW equation that describes solitary waves in a strongly nonlinear stratified fluid of finite depth is established in § 2. To gain a deeper understanding of the characteristics of solitary waves, the mass conservation and momentum conservation related to solitary waves are discussed in § 3. In § 4, by adopting Hirota's bilinear method, the bilinear form and soliton solutions of the mILW equation are obtained. Subsequently, we adopt a smooth tanh-type background density profile, and solve the corresponding Sturm–Liouville problem to determine the vertical modal functions in § 5. These modal structures are used to construct the vertical velocity field and interpret the spatial asymmetry and bottom intensification of ISWs. Finally, a summary is presented in § 6.

2. Derivation procedure of the mILW equation

In this study, we focus on the two-dimensional motion of two layers of incompressible fluids that are stratified according to density in the z direction. The governing equations (Grimshaw, Pelinovsky & Poloukhina 2002) in Eulerian coordinates are

$$\begin{cases} \dfrac{\partial u}{\partial x}+\dfrac{\partial w}{\partial z}=0, \\ \dfrac{\partial \rho}{\partial t}+u\dfrac{\partial \rho}{\partial x}+w\dfrac{\partial \rho}{\partial z}=0, \\ \rho\left(\dfrac{\partial u}{\partial t}+u\dfrac{\partial u}{\partial x}+w\dfrac{\partial u}{\partial z}\right)=-\dfrac{\partial p}{\partial x}, \\ \rho\left(\dfrac{\partial w}{\partial t}+u\dfrac{\partial w}{\partial x}+w\dfrac{\partial w}{\partial z}\right)=-\dfrac{\partial p}{\partial z}-g\rho. \end{cases} \tag{2.1}$$

Here, the horizontal coordinate axis is at the interface between the two fluid layers, with the vertical axis z being positive in the upward direction. The velocity components in the x and z directions are represented by u and w, respectively; ρ denotes the density, t is the time variable, p represents the fluid pressure, and g is the acceleration due to gravity. Equation (2.1) have a solution corresponding to a motionless ground state, where $u=u_0=0$, $v=v_0=0$, $p=p_0(z)$, $\rho=\rho_0(z)$. The fundamental hydrostatic equilibrium is described by $\mathrm{d}p_0/\mathrm{d}z=-g\rho_0$. The appropriate boundary conditions associated with $w(z)$ are $w=0$ when $z=h$ and $z=-H$.

This study investigates the unsteady propagation of nonlinear water waves in a density-stratified fluid system. We adopt a tanh-type continuous density profile (Lamb & Xiao 2014) to model the structure characteristic of stratified oceans, where the interface at $z=0$ ensures smooth density continuity:

$$\rho_0\,(z)=\begin{cases} \rho_0(z), & h\geqslant z>0, \\ \rho_0(0)=\text{constant}, & 0\geqslant z\geqslant -H. \end{cases} \tag{2.2}$$

Specifically, the density distribution is defined such that the upper layer ($h\geqslant z>0$) exhibits a vertical variation in density, while the lower layer ($0\geqslant z\geqslant -H$) remains

https://doi.org/10.1017/jfm.2025.10719 Published online by Cambridge University Press

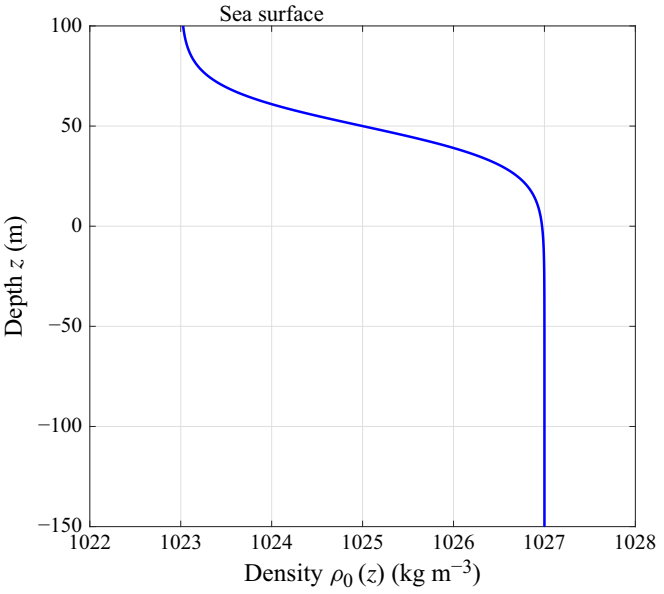


Figure 1. Stratified ocean density profile.

homogeneous with constant density ρ_0. Figure 1 illustrates the schematic of the density profile model.

In the derivation of the classical model describing ISWs, Benjamin (1967) brought in a small parameter ϵ. This parameter was used to represent the wave motion at a characteristic spatial scale of the same order as the nonlinearity to balance the effects of nonlinearity and dispersion. However, as the scope of research expanded to include real-world oceanic scenarios with a wider range of wave amplitudes, a significant issue emerged. As the amplitude of the solitary wave increases, the influence of the higher-order nonlinear terms gradually intensifies, resulting in an imbalance between the nonlinear and dispersion effects. When dealing with large-amplitude ISWs, the existing model becomes increasingly inadequate. It fails to accurately capture stronger nonlinear effects or complex soliton dynamics such as modulation instability and high-order soliton interactions. To overcome these limitations and develop a more accurate model that can better account for the behaviour of large-amplitude ISWs, we introduce the following Gardner–Morikawa type transformation in the region $h \geqslant z > 0$ (Gardner & Morikawa 1965; Yu, Fu & Yang 2021):

$$T = \epsilon^{\frac{3}{2}} t, \quad X = \epsilon^{\frac{1}{2}} (x - t). \tag{2.3}$$

Here, both T and X are slow variables, where T denotes the temporal coordinate, and X represents the spatial coordinate. In this way, we obtain the relationship

$$\frac{\partial}{\partial t} = \epsilon^{\frac{3}{2}} \frac{\partial}{\partial T} - \epsilon^{\frac{1}{2}} \frac{\partial}{\partial X}, \quad \frac{\partial}{\partial x} = \epsilon^{\frac{1}{2}} \frac{\partial}{\partial X}. \tag{2.4}$$

The perturbation method is a fundamental analytical technique in water wave research (Michele & Renzi 2020). The essence of the perturbation method is that the complex equations describing a nonlinear wave are reduced to a simple and solvable nonlinear equation by appropriate reductive perturbation expansion. Here, we assume that the velocity components u, w, and pressure p and density ρ, can be asymptotically expanded in terms of a small parameter ϵ, reflecting their hierarchical contributions across

https://doi.org/10.1017/jfm.2025.10719 Published online by Cambridge University Press

multiple scales. Specifically, these variables are represented as a series of successive approximations:

$$\begin{cases} u(X,z,T)=\displaystyle\sum_{i=1}^{n}\epsilon^{\frac{i}{2}}\,u_i(X,z,T),\\ w(X,z,T)=\displaystyle\sum_{i=1}^{n}\epsilon^{\frac{i+1}{2}}\,w_i(X,z,T),\\ p(X,z,T)=p_0(z)+\displaystyle\sum_{i=1}^{n}\epsilon^{\frac{i}{2}}\,p_i(X,z,T),\\ \rho(X,z,T)=\rho_0(z)+\displaystyle\sum_{i=1}^{n}\epsilon^{\frac{i}{2}}\,\rho_i(X,z,T), \end{cases} \tag{2.5}$$

where the subscript indices denote the order of the perturbation terms. This expansion systematically captures the interplay between nonlinear and dispersive effects, ensuring a balanced representation of dominant and higher-order dynamics.

To systematically derive the governing equations, we begin by substituting (2.4) and (2.5) into the fundamental system (2.1). This yields the lowest-order approximate equations for the perturbation parameter ϵ:

$$\begin{cases} \dfrac{\partial\rho_1}{\partial X}-w_1\dfrac{\mathrm{d}\rho_0}{\mathrm{d}z}=0,\\ \dfrac{\partial u_1}{\partial X}+\dfrac{\partial w_1}{\partial z}=0,\\ -\rho_0\dfrac{\partial u_1}{\partial X}+\dfrac{\partial p_1}{\partial X}=0,\\ \dfrac{\partial p_1}{\partial z}=-g\rho_1. \end{cases} \tag{2.6}$$

Through algebraic elimination of variables p_1, u_1, ρ_1, we isolate the governing equation for w_1:

$$\frac{\partial}{\partial z}\left(\rho_0\frac{\partial w_1}{\partial z}\right)-g w_1\frac{\mathrm{d}\rho_0}{\mathrm{d}z}=0. \tag{2.7}$$

A separation-of-variables approach is then applied to (2.7), assuming solutions of the form

$$w_1(X,z,T)=-\phi_1(z)\,f_X(X,T), \tag{2.8}$$

where the subscript X denotes a partial derivative with respect to the stretched coordinate X. Substituting (2.8) into (2.6) simplifies the analysis, and it is easy to find that

$$u_1=f\frac{\mathrm{d}\phi_1}{\mathrm{d}z},\quad p_1=\rho_0\frac{\mathrm{d}\phi_1}{\mathrm{d}z}f,\quad \rho_1=-\phi_1\frac{\mathrm{d}\rho_0(z)}{\mathrm{d}z}f. \tag{2.9}$$

Further, the next-order approximate equations for ϵ can be derived as

https://doi.org/10.1017/jfm.2025.10719 Published online by Cambridge University Press

$$\begin{cases} -\dfrac{\partial \rho_2}{\partial X} + w_2 \dfrac{\partial \rho_0}{\partial z} = A_1 = u_1 \dfrac{\partial \rho_1}{\partial X}, \\ \dfrac{\partial u_2}{\partial X} + \dfrac{\partial w_2}{\partial z} = 0, \\ -\rho_0 \dfrac{\partial u_2}{\partial X} + \dfrac{\partial p_2}{\partial X} = A_2 = -\rho_0 u_1 \dfrac{\partial u_1}{\partial X} - \rho_0 w_1 \dfrac{\partial u_1}{\partial z}, \\ \dfrac{\partial p_2}{\partial z} = -g\rho_2, \end{cases} \tag{2.10}$$

leading to the governing equation for w_2:

$$\frac{\partial}{\partial z}\left(\rho_0 \frac{\partial w_2}{\partial z}\right) - g w_2 \frac{\mathrm{d}\rho_0}{\mathrm{d}z} = -g A_1 + \frac{\partial A_2}{\partial z}. \tag{2.11}$$

Here,

$$\begin{aligned} A_1 &= u_1 \frac{\partial \rho_1}{\partial X} = -\phi_1 \frac{\mathrm{d}\phi_1}{\mathrm{d}z} \frac{\mathrm{d}\rho_0}{\mathrm{d}z} f f_X, \\ A_2 &= -\rho_0 u_1 \frac{\partial u_1}{\partial X} - \rho_0 w_1 \frac{\partial u_1}{\partial z} = \left[-\rho_0^2 \left(\frac{\mathrm{d}\phi_1}{\mathrm{d}z}\right)^2 + \rho_0 \phi_1 \frac{\mathrm{d}^2 \phi_1}{\mathrm{d}z^2} \right] f f_X. \end{aligned} \tag{2.12}$$

As a result, we can assume the functional form

$$w_2 = \phi_2(z)\, f(X, T)\, f_X(X, T), \tag{2.13}$$

and p_2, u_2 and ρ_2 can be solved:

$$\begin{cases} u_2 = -f^2 \dfrac{\mathrm{d}\phi_2}{\mathrm{d}z}, \\ \rho_2 = \dfrac{\mathrm{d}\rho_0}{\mathrm{d}z}\left(\phi_2 + \phi_1 \dfrac{\mathrm{d}\phi_1}{\mathrm{d}z}\right) f^2, \\ p_2 = \left(-g \displaystyle\int \frac{\mathrm{d}\rho_0}{\mathrm{d}z}\left(\phi_2 + \phi_1 \frac{\mathrm{d}\phi_1}{\mathrm{d}z}\right) \mathrm{d}z\right) \times f^2. \end{cases} \tag{2.14}$$

Finally, we can obtain

$$\begin{cases} -\dfrac{\partial \rho_3}{\partial X} + w_3 \dfrac{\partial \rho_0}{\partial z} = B_1, \\ \dfrac{\partial u_3}{\partial X} + \dfrac{\partial w_3}{\partial z} = 0, \\ -\rho_0 \dfrac{\partial u_3}{\partial X} + \dfrac{\partial p_3}{\partial X} = B_2, \\ \dfrac{\partial p_3}{\partial z} + g\rho_3 = B_3, \end{cases} \tag{2.15}$$

where

$$\begin{cases} B_1 = u_1 \dfrac{\partial \rho_2}{\partial X} + u_2 \dfrac{\partial \rho_1}{\partial X}, \\ B_2 = -\rho_0 \dfrac{\partial u_1}{\partial T} - \rho_0 u_1 \dfrac{\partial u_2}{\partial X} - \rho_0 u_2 \dfrac{\partial u_1}{\partial X} - w_1 \dfrac{\partial u_2}{\partial z} - w_2 \dfrac{\partial u_1}{\partial z}, \\ B_3 = \rho_0 \dfrac{\partial w_1}{\partial X}. \end{cases} \tag{2.16}$$

https://doi.org/10.1017/jfm.2025.10719 Published online by Cambridge University Press

Subsequently eliminating u_3, ρ_3 and p_3, the governing equation for w_3 is

$$\frac{\partial}{\partial z}\left(\rho_0\frac{\partial w_3}{\partial z}\right)-g w_3\frac{\mathrm{d}\rho_0}{\mathrm{d}z}=C, \tag{2.17}$$

where

$$C=-\frac{\partial B_3}{\partial X}-g B_1+\frac{\partial B_2}{\partial z}. \tag{2.18}$$

Substituting (2.16) into (2.18) yields

$$C=C_1 f_T+C_2 f_{XXX}+C_3 f^2 f_X, \tag{2.19}$$

with

$$\begin{cases} C_1=-\dfrac{\mathrm{d}}{\mathrm{d}z}\left(\rho_0\dfrac{\mathrm{d}\phi_1}{\mathrm{d}z}\right), \quad C_2=\rho_0\phi_1, \\ C_3=-g\dfrac{\mathrm{d}\rho_0}{\mathrm{d}z}\left[2\dfrac{\mathrm{d}\phi_1}{\mathrm{d}z}\phi_2+\phi_1\left(\dfrac{\mathrm{d}\phi_1}{\mathrm{d}z}\right)^2+\dfrac{\mathrm{d}\phi_2}{\mathrm{d}z}\phi_1\right] \\ \qquad -\dfrac{\mathrm{d}}{\mathrm{d}z}\left(\rho_0\dfrac{\mathrm{d}\phi_1}{\mathrm{d}z}\dfrac{\mathrm{d}\phi_2}{\mathrm{d}z}+\phi_1\dfrac{\mathrm{d}^2\phi_2}{\mathrm{d}z^2}+\phi_2\dfrac{\mathrm{d}^2\phi_1}{\mathrm{d}z^2}\right). \end{cases} \tag{2.20}$$

Multiplying both sides of (2.17) by ϕ_1, and integrating over z in $[0,\,h]$, we can obtain

$$\left[\rho_0\left(\phi_1\frac{\mathrm{d}w_3}{\mathrm{d}z}-\frac{\mathrm{d}\phi_1}{\mathrm{d}z}w_3\right)\right]\Bigg|_{z=0}^{h}=\int_0^h C\phi_1\,\mathrm{d}z, \tag{2.21}$$

where $\phi_1(h)=0$ at $z=h$. Incorporating (2.19) into (2.21) yields a compatibility condition for the perturbation hierarchy:

$$\left[\rho_0\left(\phi_1\frac{\mathrm{d}w_3}{\mathrm{d}z}-\frac{\mathrm{d}\phi_1}{\mathrm{d}z}w_3\right)\right]\Bigg|_{z=0}^{h}=a_1 f_T+a_2 f_{XXX}+a_3 f^2 f_X, \tag{2.22}$$

where

$$\begin{cases} a_1=\displaystyle\int_0^h\left[\phi_1\frac{\mathrm{d}}{\mathrm{d}z}\left(\rho_0\frac{\mathrm{d}\phi_1}{\mathrm{d}z}\right)\right]\mathrm{d}z, \\ a_2=\displaystyle\int_0^h\left(\rho_0\phi_1^2\right)\mathrm{d}z, \\ a_3=\displaystyle\int_0^h-\left\{\phi_1\frac{\mathrm{d}}{\mathrm{d}z}\left(\rho_0\frac{\mathrm{d}\phi_1}{\mathrm{d}z}\frac{\mathrm{d}\phi_2}{\mathrm{d}z}+\phi_1\frac{\mathrm{d}^2\phi_2}{\mathrm{d}z^2}+\phi_2\frac{\mathrm{d}^2\phi_1}{\mathrm{d}z^2}\right)\right\}\mathrm{d}z \\ \qquad -\displaystyle\int_0^h\left\{g\phi_1\frac{\mathrm{d}\rho_0}{\mathrm{d}z}\left[2\frac{\mathrm{d}\phi_1}{\mathrm{d}z}\phi_2+\phi_1\left(\frac{\mathrm{d}\phi_1}{\mathrm{d}z}\right)^2+\frac{\mathrm{d}\phi_2}{\mathrm{d}z}\phi_1\right]\right\}\mathrm{d}z. \end{cases} \tag{2.23}$$

In order to capture the multi-scale nature of ISWs in a two-layer ocean, we introduce scaled coordinates that reflect the distinct dynamical behaviours of the upper and lower layers. The upper layer, typically characterised by a thinner depth and smaller density, exhibits faster wave propagation and stronger nonlinear effects, necessitating a finer horizontal scaling. In contrast, the lower layer, with its greater depth and larger density, supports waves with a broader horizontal scale and slower dynamics. To balance the nonlinear and dispersive effects in both layers, we adopt different scaling for the horizontal coordinate in the upper and lower layers, while maintaining a consistent time scaling to

https://doi.org/10.1017/jfm.2025.10719 Published online by Cambridge University Press

ensure the synchronisation of wave evolution across the interface. Specifically, in the lower layer $0 \geqslant z \geqslant -H$, we adopt the stretching transformations

$$T = \epsilon^{\frac{3}{2}} t, \quad X = x - t. \tag{2.24}$$

This is expressible as

$$\frac{\partial}{\partial t} = \epsilon^{\frac{3}{2}} \frac{\partial}{\partial T} - \frac{\partial}{\partial X}, \quad \frac{\partial}{\partial x} = \frac{\partial}{\partial X}. \tag{2.25}$$

Asymptotic expansions for u, w, p, ρ are then formulated as

$$\begin{cases} u(X, z, T) = \displaystyle\sum_{i=1}^{n} \epsilon^{\frac{i+1}{2}} U_i(X, z, T), \\ w(X, z, T) = \displaystyle\sum_{i=1}^{n} \epsilon^{\frac{i+1}{2}} W_i(X, z, T), \\ p(X, z, T) = p_0(z) + \displaystyle\sum_{i=1}^{n} \epsilon^{\frac{i+1}{2}} P_i(X, z, T), \\ \rho(X, z, T) = \rho_0(z). \end{cases} \tag{2.26}$$

Substituting (2.25) and (2.26) into (2.1), Laplace's equation for W_1 can be expressed as

$$\frac{\partial^2 W_1}{\partial X^2} + \frac{\partial^2 W_1}{\partial z^2} = O(\epsilon), \tag{2.27}$$

with boundary conditions

$$\begin{aligned} W_1(X, z, T) &= W_0, \qquad z = 0, \\ W_1(X, z, T) &= 0, \qquad z = -H. \end{aligned}$$

Since (2.27) is Laplace's equation, by applying the Fourier transform, its inverse transform and the convolution theorem, we are able to obtain the solution of (2.27):

$$W_1(X, z, T) = \frac{1}{2\pi} \int_{-\infty}^{+\infty} \mathcal{F}\left(W_1|_{z=0}\right) \frac{\mathrm{e}^{-kz} - \mathrm{e}^{2kH+kz}}{1 - \mathrm{e}^{2kH}} \mathrm{e}^{\mathrm{i}kX} \, \mathrm{d}k. \tag{2.29}$$

Here, $\mathcal{F}(W_1|_{z=0})$ represents the Fourier transformation of $W_1|_{z=0}$. Differentiating (2.29) with respect to z gives

$$\frac{\partial W_1(X, z, T)}{\partial z} = -\frac{1}{2\pi} \int_{-\infty}^{+\infty} k \, \mathcal{F}\left(W_1|_{z=0}\right) \frac{1 + \mathrm{e}^{2kH+2kz}}{(1 - \mathrm{e}^{2kH}) \, \mathrm{e}^{kz}} \mathrm{e}^{\mathrm{i}kX} \, \mathrm{d}k. \tag{2.30}$$

To establish the continuity condition at the interface $z = 0$, the solutions of the upper and lower layers are matched. Since the lower fluid in our model is specified as a homogeneous medium, pressure continuity automatically holds under this configuration. At the interface $z = 0$, we impose matching conditions based on the continuity of vertical velocity. These arise naturally from the requirement that the fluid motion be dynamically and kinematically compatible across the interface. In particular, since the density is assumed to be continuous at the interface, and the fluids are incompressible, the vertical velocity must also be continuous at $z = 0$. This ensures the smooth transmission of internal wave energy and momentum between the two layers, and is physically justified. By taking

https://doi.org/10.1017/jfm.2025.10719 Published online by Cambridge University Press

the limit as z approaches zero, the following relationships are derived:

$$\epsilon w_1|_{z=0} + \epsilon^{\frac{3}{2}} w_2\Big|_{z=0} + \epsilon^2 w_3\Big|_{z=0} = \epsilon W_1|_{z=0}\,, \tag{2.31}$$

$$\epsilon \frac{\partial w_1}{\partial z}\Big|_{z=0} + \epsilon^{\frac{3}{2}} \frac{\partial w_2}{\partial z}\Big|_{z=0} + \epsilon^2 \frac{\partial w_3}{\partial z}\Big|_{z=0} = \epsilon \frac{\partial W_1}{\partial z}\Big|_{z=0}. \tag{2.32}$$

From (2.31), we can get

$$-\phi_1(z)\ f_X|_{z=0} = W_1|_{z=0}\,, \quad w_3|_{z=0} = 0. \tag{2.33}$$

According to (2.30) and (2.33), we have

$$\frac{\partial W_1}{\partial z} = \frac{-\epsilon}{4H}\frac{\partial^2}{\partial X^2}\int_{-\infty}^{+\infty} f(X', T)\,\phi_1(0)\coth\left[\frac{\pi}{4H}(X' - X)\right]\mathrm{d}X'. \tag{2.34}$$

Considering (2.8), (2.32) and (2.34), it is easy to find that

$$\begin{aligned} &\phi_1(0) = 1, \quad \frac{\partial \phi_1}{\partial z}\Big|_{z=0} = 0, \quad w_3(0) = 0, \\ &\frac{\partial w_3}{\partial z}\Big|_{z=0} = \frac{-1}{4H}\frac{\partial^2}{\partial X^2}\int_{-\infty}^{+\infty} f(X', T)\,\phi_1(0)\coth\left[\frac{\pi}{4H}(X' - X)\right]\mathrm{d}X'. \end{aligned} \tag{2.35}$$

Next, substituting (2.35) into (2.22), the new governing equation is obtained:

$$f_T + b_1 f^2 f_X + b_2 f_{XXX} + b_3 \frac{\partial^2}{\partial X^2}\mathrm{G}(f) = 0, \tag{2.36}$$

with $\mathrm{G}(f) = (-1/(4H))(\partial^2/\partial X^2)\int_{-\infty}^{+\infty} f(X', T)\,\phi_1(0)\coth[(\pi/(4H))(X' - X)]\,\mathrm{d}X'$, $b_1 = (a_2/a_1)$, $b_2 = (a_3/a_1)$, $b_3 = (\rho_0(-h)/a_1)$.

Equation (2.36) is a modified model, designated as the mILW equation, which is introduced here to model ISWs in oceanic environments. For brevity, (2.36) is referred to as the mILW model. When the dispersive term f_{xxx} vanishes, the mILW equation reduces to the cubic ILW (cILW) equation, as discussed in Naumkin & Sánchez-Suárez (2018). It reduces to the classical ILW equation when the dispersive term f_{XXX} vanishes and the nonlinear term $f^2 f_X$ simplifies to $f f_X$, as documented in Joseph (1977) and Kubota *et al.* (1978). And when the integral term has $b_3 = 0$, it simplifies to the mKdV equation.

The KdV equation is suited for shallow water with weak nonlinearity and long waves. The BO equation assumes an infinitely deep lower layer and is valid for interfacial waves with non-local dispersion, but it lacks applicability in finite-depth ocean environments. The ILW equation bridges the above models by capturing non-local dispersive effects in finite-depth stratified fluids, making it more versatile for oceanographic applications.

Nevertheless, the standard ILW equation includes only quadratic nonlinearity and cannot fully describe the complex structure of stronger nonlinear solitary waves. The mILW equation developed in this work incorporates a third-order nonlinear correction term, enabling the capture of stronger nonlinear behaviours such as amplitude-dependent wave deformation and asymmetrical profiles that are frequently observed in oceanic solitary waves, which are worth further study.

3. Conservation laws

Conservation laws are fundamental to the study of solitary waves, providing critical insights into the underlying dynamics of unsteady wave propagation. These laws, which describe the preservation of quantities such as mass, momentum and energy, are of

https://doi.org/10.1017/jfm.2025.10719 Published online by Cambridge University Press

profound significance in mathematical physics and fluid mechanics, offering a robust framework for analysing wave behaviour and stability (Cebeci & Bradshaw 1984; Abreu *et al.* 2024).

Building on this foundation, we now turn our attention to identifying conserved quantities for (2.36). By systematically examining the structure of the equation, we aim to derive conservation laws that elucidate the energy and momentum transfer mechanisms inherent in the system.

Assuming that $f(X,T)$ and its derivatives $f_X(X,T)$, $f_{XX}(X,T)$ and $f_{XXX}(X,T)$ approach zero as $|X|\to\infty$, the conservation of mass is first examined. Equation (2.36) is reformulated as

$$f_T = -b_1 f_{XXX} - b_2 f^2 f_X - b_3 \frac{\partial^2}{\partial X^2}\,\mathrm{G}(f), \tag{3.1}$$

and integrating (3.1) with respect to X over the interval $(-\infty,\infty)$ yields

$$\frac{\mathrm{d}}{\mathrm{d}T}\int_{-\infty}^{+\infty} f\,\mathrm{d}X = 0. \tag{3.2}$$

Furthermore, multiplying (3.1) by f and rearranging,

$$f f_T = -b_1 f f_{XXX} - b_2 f^3 f_X - b_3 f \frac{\partial^2}{\partial X^2}\,\mathrm{G}(f), \tag{3.3}$$

integrating (3.3) about X from $-\infty$ to ∞, and utilising the following properties of the Hilbert operator,

$$\begin{gathered}\frac{\partial^2}{\partial X^2}\mathrm{G}(f) = \mathrm{G}\left(\frac{\partial^2 f}{\partial X^2}\right),\\ \int_{-\infty}^{+\infty} f\mathrm{G}f\,\mathrm{d}X = 0,\\ \int_{-\infty}^{+\infty} f\mathrm{G}g\,\mathrm{d}X = -\int_{-\infty}^{+\infty} g\mathrm{G}f\,\mathrm{d}X,\end{gathered} \tag{3.4}$$

yields

$$\frac{\mathrm{d}}{\mathrm{d}T}\int_{-\infty}^{+\infty} f^2\,\mathrm{d}X = 0, \tag{3.5}$$

and the expression for mass M_1,

$$M_1 = \int_{-\infty}^{+\infty} \rho\,\mathrm{d}X, \tag{3.6}$$

where

$$\rho(X,z,T) = \rho_0(z) + \epsilon^{\frac{1}{2}}\,\rho_1(X,z,T) + \epsilon\,\rho_2(X,z,T). \tag{3.7}$$

It is known above that $\rho_2 = (\mathrm{d}\rho_0/\mathrm{d}z)(\phi_2 + \phi_1(\mathrm{d}\phi_1/\mathrm{d}z))f^2$, $\rho_1 = -\phi_1(\mathrm{d}\rho_0(z)/\mathrm{d}z)f$, so the mass conservation can be obtained:

$$\frac{\mathrm{d}M_1}{\mathrm{d}T} = 0. \tag{3.8}$$

Similarly, momentum conservation law can be investigated:

$$M_2 = \int_{-\infty}^{+\infty} \rho w\,\mathrm{d}X, \tag{3.9}$$

https://doi.org/10.1017/jfm.2025.10719 Published online by Cambridge University Press

where

$$\begin{aligned} w(X, z, T) &= \epsilon\, w_1(X, z, T) + \epsilon^{\frac{3}{2}}\, w_2(X, z, T), \\ w_1(X, z, T) &= -\phi_1(z)\, f_X(X, T), \\ w_2(X, z, T) &= \phi_2(z)\, f(X, T)\, f_X(X, T), \end{aligned} \tag{3.10}$$

so the law of momentum conservation can be derived as

$$\frac{\mathrm{d}M_2}{\mathrm{d}T} = 0, \tag{3.11}$$

with

$$\begin{aligned} M_2 &= \int_{-\infty}^{+\infty} \left[\beta_1 f_X + \beta_2 f f_X + \beta_3 f^2 f_X + \beta_4 f^3 f_X\right] \mathrm{d}X, \\ \beta_1 &= -\epsilon\, \rho_0(z)\, \phi_1(z), \\ \beta_2 &= \epsilon^{\frac{3}{2}}\, \rho_0(z)\, \phi_2(z) - \epsilon\alpha_1\, \phi_1(z), \\ \beta_3 &= -\epsilon^{\frac{3}{2}}\alpha_1\, \phi_2(z) - \epsilon\alpha_2\, \phi_1(z), \\ \beta_4 &= -\epsilon^{\frac{3}{2}}\alpha_2\, \phi_2(z). \end{aligned} \tag{3.12}$$

This analysis provides a comprehensive understanding of the model's conservation properties. In the context of nonlinear wave models, conservation laws not only validate the mathematical consistency of the governing equations, but also facilitate the derivation of analytical solutions and the interpretation of physical phenomena. These conserved quantities will serve as essential tools for understanding the stability and long-term behaviour of the wave solutions described by the model.

4. Bilinear form and soliton solutions

To gain deeper insights into the propagation dynamics of ISWs, it is essential to solve the nonlinear governing equation (2.36). The study of nonlinear evolution equations has long been a central theme in applied mathematics and theoretical physics, driving the development of numerous analytical and numerical techniques. Hirota's bilinear method is a powerful tool for constructing multi-soliton solutions for equations of nonlinear evolution. By transforming the nonlinear equation into a bilinear framework through an appropriate variable transformation, Hirota's bilinear method enables the systematic construction of multi-soliton solutions, making it a cornerstone of soliton theory and nonlinear dynamics. In this section, we employ this method to derive the bilinear form and soliton solutions of (2.36).

The bilinear method has found widespread applications across diverse fields, including mathematical physics, fluid dynamics and optical solitons, due to its ability to handle complex nonlinear interactions with remarkable efficiency. To ensure the physical relevance of the solutions, we impose the condition that the wave profile remains real and finite for all values of the spatial coordinate X and time T. Under this assumption, the solution can be expressed in the form

$$f(X, T) = \mathrm{i}\, \frac{\partial}{\partial X} \ln \frac{g^+(X, T)}{g^-(X, T)}, \tag{4.1}$$

where

$$g^+(X, T) = g(X - 2\mathrm{i}H, T), \quad g^-(X, T) = g(X + 2\mathrm{i}H, T), \tag{4.2}$$

https://doi.org/10.1017/jfm.2025.10719 Published online by Cambridge University Press

and satisfies $f \to 0,\ |X| \to \infty$, where

$$\begin{cases} g\,(X, Y, T) = \displaystyle\prod_{n=1}^{N} \left\{ 1 + \exp\left(\frac{1}{2H} \left[\frac{1}{2H} (\operatorname{Im} X_n) \left(X - \frac{1}{2H} \right) - X_n^* \right] \right) \right\}, \\ 0 < \dfrac{1}{2H} \operatorname{Im} X_n < \pi, \quad n = 1, 2, \ldots, N. \end{cases} \tag{4.3}$$

Here, X_n are complex-valued functions dependent on the time variable T, and X_n^* denotes the complex conjugate of X_n.

Using the formula (Yu *et al.* 2021)

$$\int_{-\infty}^{+\infty} \frac{\coth\left[\frac{\pi\lambda}{2}(X' - X)\right]}{\cosh(\lambda\gamma X') + \cos(\gamma)} \,\mathrm{d}X' = -\frac{2\lambda^{-1} \csc(\gamma) \sinh(\lambda\gamma X)}{\cosh(\lambda\gamma X) + \cos(\gamma)} \quad (0 < \gamma < \pi), \tag{4.4}$$

$\mathrm{G}(f)$ can be written as

$$\mathrm{G}\left[f\,(X, T)\right] = -\left(\frac{g_X^+}{g^+} + \frac{g_X^-}{g^-} \right) = -\frac{\partial}{\partial X} \ln\left(g^+ g^-\right). \tag{4.5}$$

By substituting (4.1) and (4.5) into (2.36), the equation obtained is

$$\mathrm{i}\frac{\partial}{\partial T}\frac{\partial}{\partial X}\ln\frac{g^+}{g^-} + \frac{b_1}{3}\frac{\partial}{\partial X}\left(\mathrm{i}\frac{\partial}{\partial X}\ln\frac{g^+}{g^-}\right)^3 + b_2\frac{\partial^3}{\partial X^3}\left(\mathrm{i}\frac{\partial}{\partial X}\ln\frac{g^+}{g^-}\right) - b_3\frac{\partial^3}{\partial X^3}\ln\left(g^+ g^-\right) = 0. \tag{4.6}$$

Integrating this equation with respect to X gives

$$\mathrm{i}\frac{\partial}{\partial T}\ln\frac{g^+}{g^-} + \frac{b_1}{3}\left(\mathrm{i}\frac{\partial}{\partial X}\ln\frac{g^+}{g^-}\right)^3 + b_2\mathrm{i}\frac{\partial^3}{\partial X^3}\left(\ln\frac{g^+}{g^-}\right) - b_3\frac{\partial^2}{\partial X^2}\ln\left(g^+ g^-\right) = 0, \tag{4.7}$$

and applying the properties of bilinear operators, we obtain

$$\begin{aligned} &\frac{\partial}{\partial X}\ln\left(\frac{f}{g}\right) = \frac{D_X f\cdot g}{fg}, \quad \frac{\partial^2}{\partial X^2}\ln\left(\frac{f}{g}\right) = \frac{D_X^2 f\cdot f}{2f^2} - \frac{D_X^2 g\cdot g}{2g^2}, \\ &\frac{\partial^3}{\partial X^3}\ln\left(\frac{f}{g}\right) = \frac{D_X^3 f\cdot g}{fg} - 3\frac{D_X^2 f\cdot g}{fg}\frac{D_X f\cdot g}{fg} + 2\left(\frac{D_X f\cdot g}{fg}\right)^3, \\ &\frac{\partial^2}{\partial X^2}\ln\left(fg\right) = \frac{D_X^2 f\cdot g}{fg} - \left(\frac{D_X f\cdot g}{fg}\right)^2, \end{aligned} \tag{4.8}$$

where

$$D_x^n D_t^m a\cdot b = \left(\frac{\partial}{\partial x} - \frac{\partial}{\partial x_1}\right)^n \left(\frac{\partial}{\partial t} - \frac{\partial}{\partial t_1}\right)^m a(x,t)\cdot b(x_1,t_1)\Big|_{x_1=x,\ t_1=t}. \tag{4.9}$$

From (4.1) and (4.5), for clarity and without restricting generality, we adopt $b_1 = 6b_2$, which can be achieved by selecting appropriate stratification parameters consistent with observed ocean conditions, as demonstrated in § 5. As a result, the bilinear equation can be derived as

https://doi.org/10.1017/jfm.2025.10719 Published online by Cambridge University Press

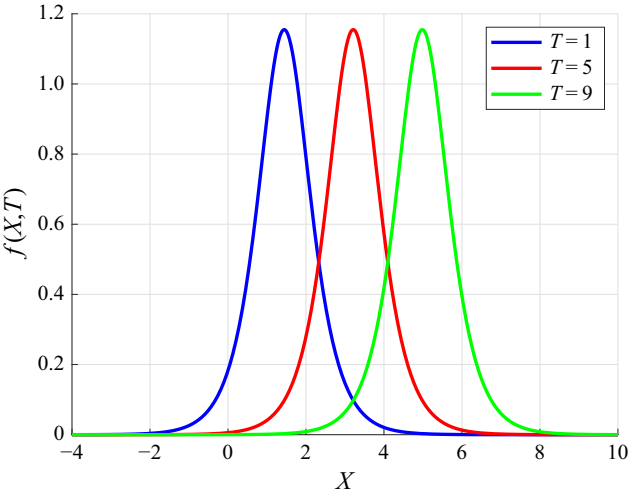


Figure 2. One-soliton solution diagrams for different time T values, with $b_1 = \pi/2,\ b_3 = \pi/6,\ k_1 = 2,\ \eta_1 = 2$.

$$\begin{aligned}\left[\mathrm{i}D_T + \frac{1}{6}b_1\mathrm{i}D_X^3 - b_3D_X^2\right]g^+g^- = 0,\\ \left[-\frac{1}{2}b_1\mathrm{i}D_X^2 + b_3D_X\right]g^+g^- = 0.\end{aligned} \tag{4.10}$$

Assuming that

$$\begin{aligned}g^+(X,T) = 1 + \epsilon g^{(1)+} + \epsilon^2 g^{(2)+} + \cdots + \epsilon^n g^{(n)+} + \cdots,\\ g^-(X,T) = 1 + \epsilon g^{(1)-} + \epsilon^2 g^{(2)-} + \cdots + \epsilon^n g^{(n)-} + \cdots,\end{aligned} \tag{4.11}$$

for a single soliton solution, substituting (4.11) into the first equation of (4.10), and comparing the coefficients of the first power of ϵ, we have

$$\epsilon:\mathrm{i}\left(g^{(1)+} - g^{(1)-}\right)_T + \frac{1}{6}b_1\mathrm{i}\left(g^{(1)+} - g^{(1)-}\right)_{XXX} - b_3\left(g^{(1)+} + g^{(1)-}\right)_{XX} = 0. \tag{4.12}$$

Equation (4.11) can be truncated to $g^{(1)+}(X,T)$ and $g^{(1)-}(X,T)$, assuming that

$$\begin{aligned}g^{(1)-} &= \mathrm{e}^{\theta_1 + \mathrm{i}\gamma_1} = \mathrm{e}^{\theta_1}(\cos\gamma_1 + \mathrm{i}\sin\gamma_1),\\ g^{(1)+} &= \mathrm{e}^{\theta_1}(\cos\gamma_1 - \mathrm{i}\sin\gamma_1),\end{aligned} \tag{4.13}$$

where $\theta_1 = k_1X + \omega_1T + \eta_1$, with k_1, ω_1, η_1 as constants. Substituting (4.13) into the bilinear equation (4.12), the dispersion relation is obtained:

$$\omega_1 = b_3k_1^2\cot\gamma_1 - \frac{1}{6}b_1k_1^3. \tag{4.14}$$

By substituting (4.13) into (4.1), the one-soliton solution of (2.36) is derived:

$$f = \frac{2k_1\,\mathrm{e}^{\theta_1}\sin\gamma_1}{1 + \mathrm{e}^{2\theta_1} + 2\mathrm{e}^{\theta_1}\cos\gamma_1}. \tag{4.15}$$

Figure 2 illustrates the one-soliton solutions at time points $T = 1, 5, 9$. Without loss of generality, parameters are selected as $b_1 = \pi/2,\ b_3 = \pi/6,\ k_1 = 2,\ \eta_1 = 2,\ \gamma_1 = \pi/3$.

https://doi.org/10.1017/jfm.2025.10719 Published online by Cambridge University Press

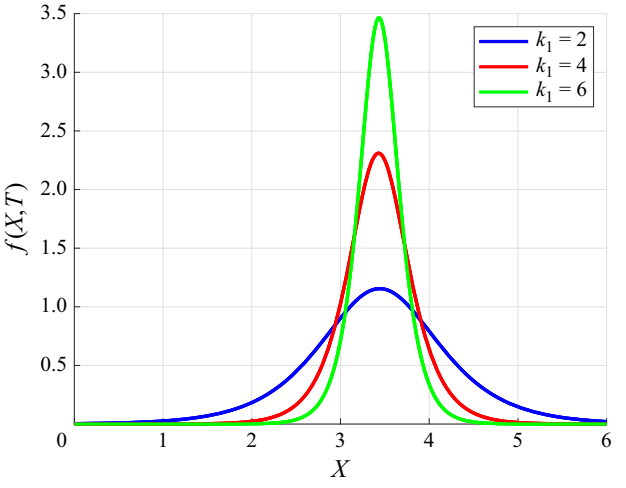


Figure 3. One-soliton solution diagrams for different k_1 values.

As depicted in figure 2, as the value of T increases, the position of the single-soliton solution exhibits a significant translation along the X-axis, while its profile shape remains largely unchanged. This indicates that under ideal conditions, where factors such as dissipation are not taken into account, it exhibits the key characteristic of shape stability during the propagation of solitons.

Figure 3 shows the influence of different $k_1 = 2, 4, 6$ values on the one-soliton solution with $b_1 = \pi/2,\ b_3 = \pi/6,\ T = 1,\ \gamma_1 = \pi/3$. From figure 3, it is clearly observed that as the wavenumber k_1 increases, the peak amplitude of the single-soliton solution curve exhibits a significant upward trend, while the curve's profile becomes steeper and sharper.

In soliton theory and related physical models, the wavenumber k_1 serves as a critical parameter that directly influences the amplitude and morphological characteristics of the single-soliton solution. By comparing the curves corresponding to different values of k_1 in figure 3, we can provide intuitive and effective visual data support for further investigating the role of wavenumber in soliton propagation and interaction processes. This analysis contributes to a deeper understanding of the dynamical behaviour of solitons under varying wavenumber conditions.

Next, we compare the soliton solution of the mILW equation with that of the ILW equation, for which we use the soliton solution found in Matsuno (1979) using Hirota's bilinear method as follows:

$$f = \lambda\gamma_1 \sin(\gamma_1) \times \left\{\cosh\left[\lambda\gamma_1\,(X - c_1 T - \delta_1)\right] + \cos\,(\gamma_1)\right\}^{-1}. \tag{4.16}$$

The parameter values are chosen to be $b_1 = \pi/6,\ b_3 = \pi/12,\ T = 2, \gamma_1 = \pi/4,\ \eta_1 = 2$. As shown in figure 4, it is evident that within the same spatial domain, the peak amplitude of the solution curve for the mILW equation is significantly higher than that for the ILW equation, indicating that the mILW model has a higher amplitude than that of the ILW model. Additionally, the gradient of the mILW solution curve is steeper, suggesting more pronounced spatial variations. This demonstrates that the mILW model exhibits stronger nonlinearity compared to the ILW model.

https://doi.org/10.1017/jfm.2025.10719 Published online by Cambridge University Press

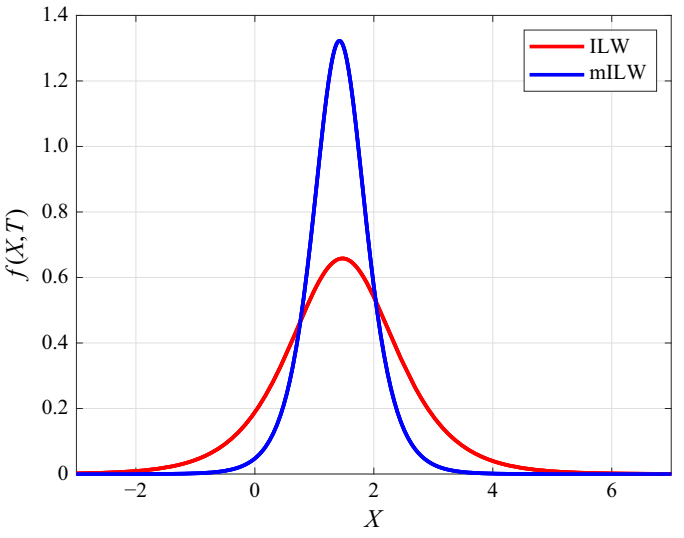


Figure 4. Comparison of the solutions of the ILW equation and the mILW equation.

For the two-soliton solution, comparing the coefficients of ϵ^2, we have

$$\epsilon^2:\begin{cases}\mathrm{i}\big(g^{(2)+}-g^{(2)-}\big)_T+\dfrac{1}{6}b_1\mathrm{i}\big(g^{(2)+}-g^{(2)-}\big)_{XXX}-b_3\big(g^{(2)+}+g^{(2)-}\big)_{XX}\\ =-\mathrm{i}\big(g_T^{(1)+}g^{(1)-}-g^{(1)+}g_T^{(1)-}\big)b_3\big(g_{XX}^{(1)+}g^{(1)-}-2g_X^{(1)+}g_X^{(1)-}+g^{(1)+}g_{XX}^{(1)-}\big)\\ -\dfrac{1}{6}b_1\mathrm{i}\big(g_{XX}^{(1)+}g^{(1)-}-g^{(1)+}g_{XXX}^{(1)-}-3g_{XX}^{(1)+}g_X^{(1)-}+3g_X^{(1)+}g_{XX}^{(1)-}\big).\end{cases}\tag{4.17}$$

We can truncate (4.10) to $g^{(2)+}(X,T)$ and $g^{(2)-}(X,T)$:

$$g^-(X,T)=1+\epsilon g^{(1)-}+\epsilon^2 g^{(2)-},\quad g^+(X,T)=1+\epsilon g^{(1)+}+\epsilon^2 g^{(2)+}.\tag{4.18}$$

Taking $g^{(1)-}=\mathrm{e}^{\theta_1+\mathrm{i}\gamma_1}+\mathrm{e}^{\theta_2+\mathrm{i}\gamma_2}$, we find that $g^{(2)-}$ is obtained as

$$g^{(2)-}=A_{12}\,\mathrm{e}^{\theta_1+\theta_2+\mathrm{i}(\gamma_1+\gamma_2)},\tag{4.19}$$

with

$$A_{12}=\frac{2\,(\omega_1-\omega_2)\sin(\gamma_1-\gamma_2)+3b_1\,(k_1-k_2)^3\sin(\gamma_1-\gamma_2)-2b_3\,(k_1-k_2)^2\cos(\gamma_1-\gamma_2)}{2\,(\omega_1+\omega_2)\sin(\gamma_1+\gamma_2)+3b_1\,(k_1+k_2)^3\sin(\gamma_1+\gamma_2)-2b_3\,(k_1+k_2)^2\cos(\gamma_1+\gamma_2)}.\tag{4.20}$$

Substituting (4.19) into (4.10), the two-soliton solution of (2.36) is

$$f=\frac{-2\,(B_2C_1-B_1C_2)}{B_1^2+B_2^2},\tag{4.21}$$

https://doi.org/10.1017/jfm.2025.10719 Published online by Cambridge University Press

h (m)	L	$\Delta\rho$ (kg m^{-3})	H (m)	a_2	a_3	a_2/a_3	Skewness	Kurtosis
98.19	4.50	0.32	162.86	1.000×10^{0}	1.667×10^{-1}	6.000000	−0.3464	5.0386
100.00	4.50	0.31	165.92	1.000×10^{0}	1.667×10^{-1}	6.000000	−0.3447	5.0380
100.00	4.50	0.49	100.00	1.000×10^{0}	1.667×10^{-1}	6.000000	−0.1981	4.9823
100.00	3.77	0.30	173.23	1.000×10^{0}	1.667×10^{-1}	6.000000	−0.3565	5.0587
99.76	4.35	0.30	170.18	1.000×10^{0}	1.667×10^{-1}	6.000000	−0.3511	5.0445
92.22	4.40	0.30	171.70	1.000×10^{0}	1.667×10^{-1}	6.000000	−0.3671	5.0526
70.06	3.23	0.44	128.69	1.000×10^{0}	1.667×10^{-1}	6.000000	−0.3786	5.0832
100.00	2.97	0.32	169.45	1.000×10^{0}	1.667×10^{-1}	6.000000	−0.3561	5.0760
100.00	4.39	0.45	114.50	1.000×10^{0}	1.667×10^{-1}	6.000000	−0.2539	4.9974
95.12	4.25	0.37	142.88	1.000×10^{0}	1.667×10^{-1}	6.000000	−0.3307	5.0334

Table 1. Top ten stratification parameter sets for which $a_2/a_3 \approx 6$.

where

$$\begin{aligned} B_1 &= 1 + \mathrm{e}^{\theta_1}\cos\gamma_1 + \mathrm{e}^{\theta_2}\cos\gamma_2 + A_{12}\,\mathrm{e}^{\theta_1+\theta_2}\cos\gamma_1+\gamma_2,\\ B_2 &= \mathrm{e}^{\theta_1}\sin\gamma_1 + \mathrm{e}^{\theta_2}\sin\gamma_2 + A_{12}\,\mathrm{e}^{\theta_1+\theta_2}\sin\gamma_1+\gamma_2,\\ C_1 &= k_1\,\mathrm{e}^{\theta_1}\cos\gamma_1 + k_2\,\mathrm{e}^{\theta_2}\cos\gamma_2 + A_{12}\,(k_1+k_2)\;\mathrm{e}^{\theta_1+\theta_2}\cos\gamma_1+\gamma_2,\\ C_2 &= k_1\,\mathrm{e}^{\theta_1}\sin\gamma_1 + k_2\,\mathrm{e}^{\theta_2}\sin\gamma_2 + A_{12}\,(k_1+k_2)\;\mathrm{e}^{\theta_1+\theta_2}\sin\gamma_1+\gamma_2. \end{aligned} \tag{4.22}$$

Similarly, one can continue to calculate the three-soliton solution and four-soliton solution of the equation. Here, we will not elaborate further on this.

5. Interaction between solitary waves

In § 4, we set $b_1 = 6b_2$. To justify the condition $b_1 = 6b_2$ adopted in the model, we conducted a systematic parameter optimisation based on realistic oceanic stratification. Specifically, we considered a two-layer density structure in which the upper layer ($h \geqslant z > 0$) exhibits a vertical variation in density, while the lower layer ($0 \geqslant z \geqslant -H$) maintains a constant background density $\rho_0(0)$. Here, $z = h$ corresponds to the ocean surface. A commonly used tanh-type density profile in oceanography is adopted, and its explicit form is given as

$$\rho_0(z) = \bar{\rho} - \Delta\rho\,\tanh\left(\frac{z - z_0}{d}\right), \tag{5.1}$$

where $\rho_0(z)$ denotes the density as a function of depth z, $\bar{\rho}$ is the mean density of seawater, typically taken as 1025 kg m^{-3}, and $\Delta\rho$ represents the density contrast. The parameter z_0 denotes the centre depth of the pycnocline, while d controls the thickness and sharpness of the stratification transition.

From (2.36), we can observe that $b_1 = a_2/a_1$ and $b_2 = a_3/a_1$. To simplify the computation, it suffices to determine the parameter sets for which $b_1/b_2 = a_2/a_3 = 6$. We utilised both grid scanning and global optimisation (particle swarm) techniques, and successfully identified multiple physically reasonable parameter sets for which $a_2/a_3 = 6$ is achieved with high precision (to within 10^{-6} relative error). Table 1 shows the ten parameter sets $a_2/a_3 = 6$.

Notably, these optimal stratifications are consistent with observed oceanic conditions (e.g. upper-layer thickness 50–100 m, density differences 0.3–0.5 kg m^{-3}). These results demonstrate that the assumption $a_2/a_3 = 6$ can be consistently realised within the

https://doi.org/10.1017/jfm.2025.10719 Published online by Cambridge University Press

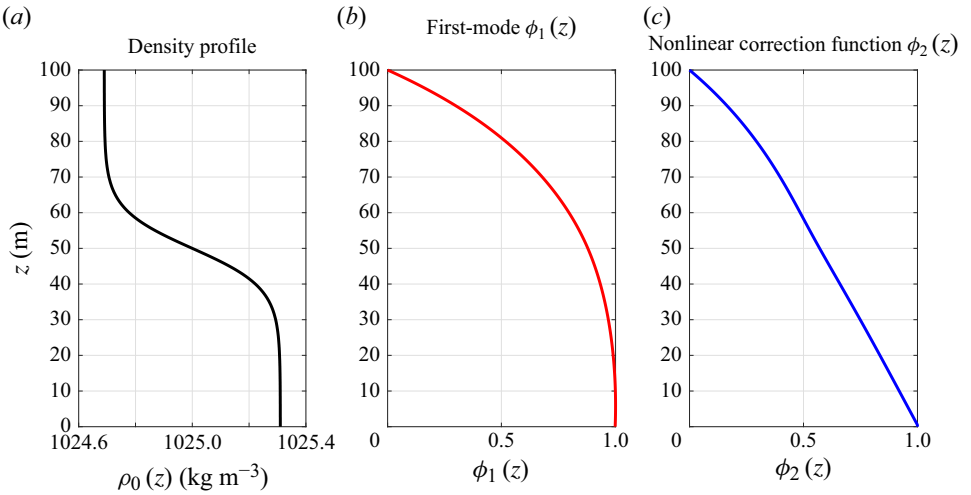


Figure 5. Density profile and vertical structure of modal functions.

framework of physically relevant stratification. Thus the use of this value in the theoretical formulation is justified, and the soliton solutions and their interaction properties discussed are based on realistic and representative oceanic environments.

Moreover, for each optimal parameter set, the computed skewness and kurtosis of the vertical velocity field provide further physical insight into the wave asymmetry and localisation induced by stratification. Specifically, we observe that the skewness values are consistently negative (approximately from -0.20 to -0.38), indicating an asymmetric wave structure characterised by enhanced downward motion beneath the pycnocline – a hallmark of nonlinear internal waves in oceanic settings. The kurtosis values range from approximately 4.98 to 5.08, significantly exceeding the Gaussian baseline 3, confirming that the wave energy is sharply concentrated around the wave crest, with heavy-tailed vertical distribution.

Importantly, both skewness and kurtosis exhibit sensitivity to stratification parameters. A larger density jump $\Delta\rho$ or sharper pycnocline (smaller L) enhances the nonlinearity of the system, which in turn leads to stronger asymmetry (more negative skewness) and sharper wave localisation (higher kurtosis). These statistical indicators thus reflect and reinforce the conclusion that the selected parameter regime supports stronger nonlinear solitary waves, and validate the capacity of the mILW model to capture essential dynamical features observed in realistic oceanic environments.

To further clarify the role of the density structure in shaping the modal dynamics and nonlinear wave behaviour, we include the computed vertical structure functions and resulting vertical velocity field in figures 5 and 6, with $h = 100$, $L = 4.5$, $\Delta\rho = 0.31$. Figure 5 illustrates the stratification profile and the corresponding vertical modal structures derived from the background density field. Figure 5(a) shows the background density $\rho_0(z)$, defined by a hyperbolic tangent function that creates a pronounced pycnocline centred at the interface $z = 0$, which separates the homogeneous lower layer from the stratified upper layer. The vertical coordinate $z \in [0, h]$ is oriented upwards, with $z = h$ at the surface.

Figure 5(b) displays the first-mode structure function $\phi_1(z)$, obtained by solving the Sturm–Liouville-type eigenvalue problem derived in § 2. In this study, we adopt a fixed boundary normalisation for the first-mode structure function $\phi_1(z)$, such that $\phi_1(h) = 0$ at the surface, and $\phi_1(0) = 1$ at the bottom of the upper fluid. This choice aligns with the theoretical framework, and ensures consistent comparison across different

https://doi.org/10.1017/jfm.2025.10719 Published online by Cambridge University Press

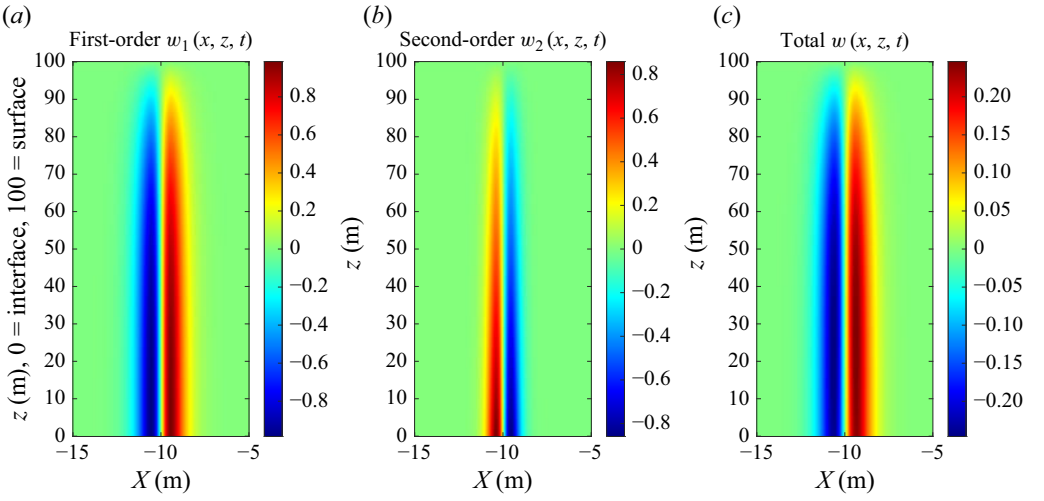


Figure 6. Vertical structure of velocity components w_1, w_2 and total field w.

stratification profiles. The resulting modal function is strictly confined within the interval [0, 1], facilitating the interpretation of vertical structure and its influence on nonlinear wave evolution. As expected, $\phi_1(z)$ increases monotonically from the surface to the bottom, representing the primary mode that governs the vertical structure of ISWs.

Figure 5(c) shows the nonlinear correction function $\phi_2(z)$, which emerges from the second-order perturbation expansion and accounts for nonlinear modifications to the wave field. Notably, the function $\phi_2(z)$ exhibits a monotonic decrease from the bottom to the surface, indicating that the nonlinear contributions are more prominent in the lower part of the stratified region. This structure introduces asymmetry into the vertical distribution of wave-induced velocity and density perturbations. This contributes to bottom intensification and asymmetrical wave profiles in strongly stratified fluids.

Figure 6 presents the vertical structure of the ISW's vertical velocity field $w(X, z, T)$, decomposed into its leading-order and second-order components derived from nonlinear theory. Figure 6(a) shows the first-order velocity component $w_1(X, z, T) = -\phi_1(z)\, f_X$, which captures the dominant structure of the wave. The velocity exhibits a symmetric dipole pattern centred around the wave crest near $X = -10$ m, with upward motion on one side, and downward motion on the other. This structure is vertically confined and aligned with the interface, diminishing towards the surface due to the boundary condition $\phi_1(h) = 0$, and reflects the classical modal shape typical of first-mode internal waves.

In contrast, figure 6(b) displays the second-order correction $w_2(X, z, T) = -\phi_2(z)\, f f_X$, which introduces clear asymmetry into the wave-induced vertical motion. The spatial pattern is notably intensified towards the lower portion of the upper layer, consistent with the shape of the second-order modal function $\phi_2(z)$, which peaks near the interface and decays upwards. This asymmetry is a hallmark of nonlinear effects in stratified fluids, where nonlinear steepening preferentially enhances velocities beneath the wave core, and suppresses upward return flow above.

Figure 6(c) combines the two contributions into the total vertical velocity field, constructed as $w = \epsilon w_1 + \epsilon^{(3/2)} w_2$, with a small nonlinearity parameter $\epsilon = 0.1$. The result is a realistic and asymmetrical wave profile that deviates from the w_1 prediction. The composite field retains the dipole character of w_1, but with skewed amplitude distribution and bottom-intensified structure, underscoring the significance of the second-order term.

https://doi.org/10.1017/jfm.2025.10719 Published online by Cambridge University Press

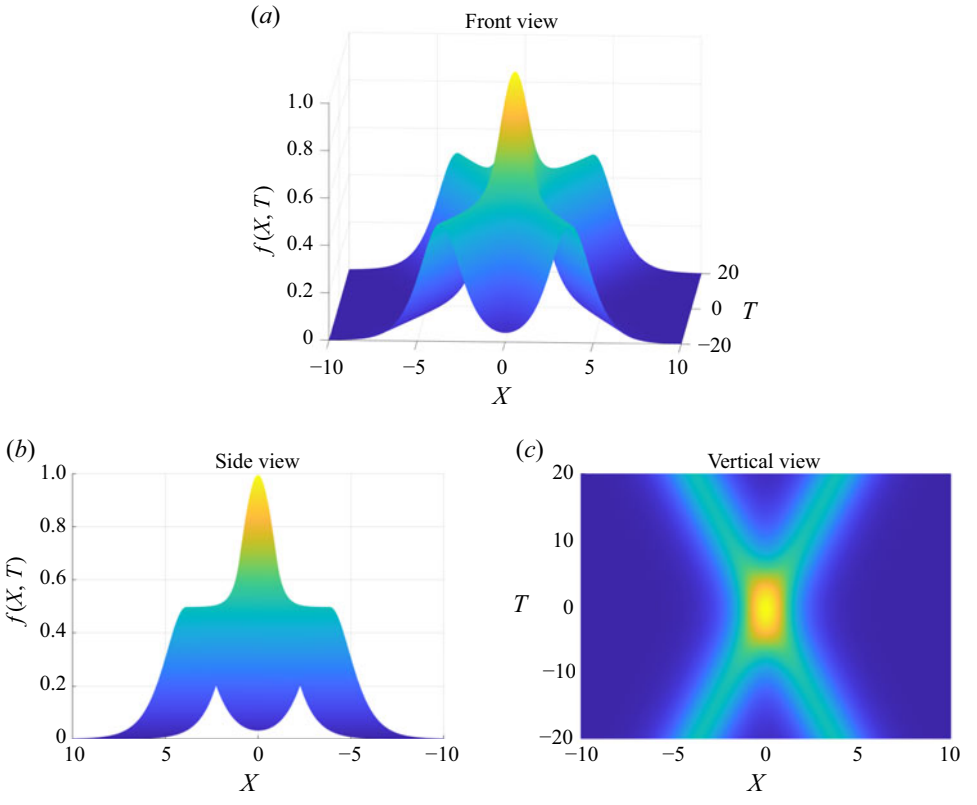


Figure 7. Illustration of the solution $f(X, T)$ with $b_1 = \pi/6$, $b_3 = \pi/12$, $k_1 = 1.2$, $\eta_1 = 0.1$: (*a*) front view, (*b*) side view, (*c*) vertical view.

These features are consistent with theoretical expectations for ISWs in stratified upper-ocean environments, and confirm the effectiveness of the mILW model in capturing both dispersive and nonlinear effects in internal wave propagation.

Building upon prior research (Yu & Song 2024), which explored the interaction of two solitary waves in the modified BO equation, this study employs a similar methodology to examine the oblique interaction of solitons within the mILW equation. Utilising the soliton solution from § 4, the interaction of two solitary waves with the same amplitude is investigated next, and the effects of the parameters k_1 and η_1 on the interaction of the solitary waves are investigated by the control variable method.

As shown in figure 7, two solitary waves with the same amplitude are placed symmetrically along the line $X = 0$. This can be expressed by the equation

$$f = \frac{2k_1\,\mathrm{e}^{k_1X+\omega_1T}\sin\gamma_1}{1+\mathrm{e}^{2(k_1X+\omega_1T)}+2\,\mathrm{e}^{k_1X+\omega_1T}\cos\gamma_1} + \frac{2k_1\,\mathrm{e}^{-k_1X+\omega_1T}\sin\gamma_1}{1+\mathrm{e}^{2(-k_1X+\omega_1T)}+2\,\mathrm{e}^{-k_1X+\omega_1T}\cos\gamma_1}. \tag{5.2}$$

The central axis effectively functions as a virtual rigid boundary. This interaction replicates the reflection pattern observed when an incident solitary wave encounters a vertical rigid wall. The highlighted region corresponds to the developing Mach stem. Under idealised, dissipation-free conditions, the collision of two solitary waves with identical amplitudes exhibits dynamics analogous to wall reflection. During this process, a reflected wave emerges and evolves into solitons matching the incident wave characteristics. Initial wave

https://doi.org/10.1017/jfm.2025.10719 Published online by Cambridge University Press



Figure 8. The interaction of oceanic ISWs (astronaut photograph STS036–082-76 acquired on 1 March 1990 at 1254 UTC), from Global Ocean Associates 2004.

overlap transforms into an amplified solitary wave structure extending along the X direction, identified as the Mach stem.

The Mach stem undergoes distinct developmental phases: initiation during wave interaction, followed by sustained growth that eventually stabilises after finite time. This characteristic evolution confirms a well-defined Mach-type reflection process.

As shown in figure 8, this type can reflect the interaction patterns in the real ocean, and was captured by the RADARSAT-1 satellite in South African waters in 1990 (Global Ocean Associates 2004). Zheng *et al.* (1997) analysed satellite imagery, and reported that both groups of ISWs propagate shorewards. When these wave packets intersect, complex nonlinear interactions are observed.

As shown in figure 9(a,b,d,e), if the wavenumber k_1 is kept constant and only the initial phase η_1 is changed, then the interaction time of the two solitary waves and the shape of the stem remain unchanged, but with the increase of η_1, the interaction time of the two solitary waves is delayed. Keeping the value of the initial phase η_1 constant and changing the value of the wavenumber k_1, as shown in figure 9(a,c,d,f), the time taken for the two solitary waves to interact becomes shorter, and the amplitude of the stem increases but their widths become narrower as the wavenumber k increases.

6. Conclusions

This study advances the theoretical and numerical understanding of ISWs in finite-depth oceans by deriving a unified framework – the mILW equation – and exploring its dynamical implications.

Rooted in the Navier–Stokes equations and developed through multi-scale analysis and perturbation methods, the mILW equation generalises classical models by incorporating higher-order nonlinearities, thereby enabling the description of large-amplitude ISWs that dominate transitional depth regimes. Its ability to reduce to the mKdV equation in the shallow-water limit and the modified BO equation in the deep-water limit demonstrates its versatility and wide-ranging applicability across different ocean depth scenarios.

The discussion of the conservation laws of the mILW model, specifically mass conservation and momentum conservation, provides a fundamental understanding of the physical properties underlying the propagation of ISWs. By constructing Hirota's bilinear form of the mILW equation, we successfully derived single-soliton and

https://doi.org/10.1017/jfm.2025.10719 Published online by Cambridge University Press

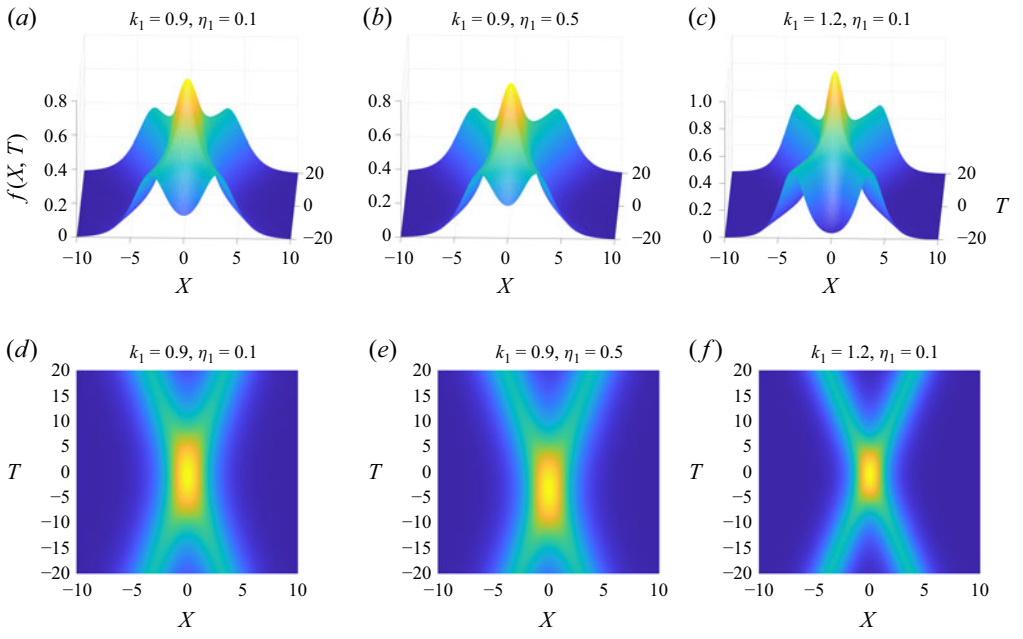


Figure 9. The interaction of solitary waves with $b_1 = \pi/6,\ b_3 = \pi/12$.

two-soliton solutions. These solutions not only enable a more detailed analysis of the propagation characteristics of ISWs, but also lay the foundation for studying more complex wave interactions.

Furthermore, a smooth tanh-type density profile is adopted to reflect realistic stratification. Associated vertical modal structures and vertical velocity fields are analysed, and higher-order statistics (skewness and kurtosis) are introduced to reveal the density dependence of wave asymmetry. The results show that under physically plausible parameter regimes, the mILW soliton exhibits pronounced asymmetry and bottom-intensified vertical structure, both of which are sensitive to the location and sharpness of the pycnocline. Skewness increases with enhanced stratification and shallower pycnocline positioning, indicating stronger nonlinear deformation of the wave profile. Similarly, elevated kurtosis values reflect the emergence of sharper and more localised wave crests. These statistical indicators confirm that the mILW model effectively captures the stratification-induced modulation of wave morphology, providing physically interpretable metrics for connecting theoretical predictions with observational data.

Our investigation into the oblique interaction of two solitary waves has uncovered important phenomena such as rogue waves and Mach reflection. These discoveries enhance our understanding of the complex dynamics that can occur during wave–wave interactions in the ocean. The numerical simulations of the effects of initial phase and wavenumber on soliton interactions have revealed distinct impacts. Changes in the initial phase only affect the timing of the soliton interactions, while variations in wavenumber significantly influence the interaction dynamics. This knowledge is particularly useful for predicting and understanding the behaviour of large-amplitude waves, including shallow-water tsunamis, in real-world ocean environments.

In summary, this research contributes to the theoretical framework of ISW propagation, and provides practical insights for ocean engineering, coastal protection and tsunami warning systems. Future research could focus on further validating the mILW equation

https://doi.org/10.1017/jfm.2025.10719 Published online by Cambridge University Press

through field observations, exploring more complex multi-soliton interactions, and extending the model to incorporate additional physical factors such as ocean stratification and topography.

Funding. This work is supported by the National Key Research and Development Programme of China (grant no. 2023YFC3008202).

Declaration of interests. The authors report no conflict of interest.

References

Abreu, E., Valencia-Guevara, J.C., Huacasi-Machaca, M. & Perez, J. 2024 A numerical scheme for doubly nonlocal conservation laws. *Calcolo* **61**, 72.

Adem, A.R. & Khalique, C.M. 2013 Exact solutions and conservation laws of a two-dimensional integrable generalization of the Kaup–Kupershmidt equation. *J. Appl. Maths* **2013**, 647313.

Benjamin, T.B. 1966 Internal waves of finite amplitude and permanent form. *J. Fluid Mech.* **25**, 241–270.

Benjamin, T.B. 1967 Internal waves of permanent form in fluids of great depth. *J. Fluid Mech.* **29**, 559–592.

Cai, S., Long, X. & Gan, Z. 2019 A numerical study of internal solitary wave evolution over a slope-shelf topography. *J. Fluid Mech.* **864**, 1–23.

Cebeci, T. & Bradshaw, P. 1984 Conservation equations for mass, momentum, and energy. In *Physical and Computational Aspects of Convective Heat Transfer*, pp. 19–40. Springer, https://doi.org/10.1007/978-3-662-02411-9_2.

Cullen, J. & Ivanov, R. 2020 On the intermediate long wave propagation for internal waves in the presence of currents. *Eur. J. Mech. B/Fluids* **84**, 325–333.

Fedele, F., Brennan, J., Ponce de León, S., Dudley, J. & Dias, F. 2016 Real world ocean rogue waves explained without the modulational instability. *Sci. Rep.* **6**, 27715.

Gardner, C.S. & Morikawa, G.K. 1965 The effect of temperature on the width of a small-amplitude, solitary wave in a collision-free plasma. *Commun. Pure Appl. Maths* **18**, 35–49.

Global Ocean Associates. 2004 An Atlas of Internal Solitary-like Waves and their Properties. https://www.internalwaveatlas.com/.

Grimshaw, R., Pelinovsky, E. & Poloukhina, O. 2002 Higher-order Korteweg–de Vries models for internal solitary waves in a stratified shear flow with a free surface. *Nonlinear Process. Geophys.* **9**, 221–235.

Guo, C. & Chen, X. 2014 A review of internal solitary wave dynamics in the northern South China Sea. *Prog. Oceanogr.* **121**, 7–23.

Han, X.F., Jin, J.R., Dong, H.H. & Fu, L. 2023 Soliton interactions and Mach reflection in gas bubbles–liquid mixures. *Phys. Fluids* **35**, 101901.

Helfrich, K.R. & Melville, W.K. 2006 Long nonlinear internal waves. *Annu. Rev. Fluid Mech.* **38**, 395–425.

Jia, Y.G., Tian, Z.C., Shi, X.F., Liu, J.P., Chen, J.X., Liu, X.L., Ye, R.J., Ren, Z.Y. & Tian, J.W. 2019 Deep-sea sediment resuspension by internal solitary waves in the northern South China Sea. *Sci. Rep.* **9**, 12137.

Joseph, R.I. 1977 Solitary waves in a finite depth fluid. *J. Phys. A: Math. Gen.* **10**, L225.

Klemas, V. & Yan, X.H. 2014 Subsurface and deeper ocean remote sensing from satellites: an overview and new results. *Prog. Oceanogr.* **122**, 1–9.

Korteweg, D.J. & de Vries, G. 1895 On the change of form of long waves advancing in a rectangular canal and on a new type of long stationary wave. *Philos. Mag.* **39**, 422–443.

Kubota, T., Ko, D.R.S. & Dobbs, L.D. 1978 Weakly-nonlinear long internal waves in a stratified fluid of finite depth. *J. Hydronaut.* **12**, 157–165.

Lamb, K.G. & Xiao, W.T. 2014 Internal solitary waves shoaling onto a shelf: comparisons of weakly-nonlinear and fully nonlinear models for hyperbolic-tangent stratifications. *Ocean Model.* **78**, 17–34.

Lamb, K.G. & Yan, L. 1996 The evolution of internal wave undular bores: comparisons of a fully nonlinear numerical model with weakly nonlinear theory. *J. Phys. Oceanogr.* **26**, 2712–2734.

Li, G.P. 2024 Deep-water and shallow-water limits of the intermediate long wave equation. *Nonlinearity* **37**, 075001.

Li, J., Xu, Z.H., Hao, Z.J., You, J., Zhang, P.W. & Yin, B.S. 2023 Internal lee wave generation from geostrophic flow in the northwestern Pacific Ocean. *J. Phys. Oceanogr.* **53**, 2633–2650.

Matsuno, Y. 1979 Exact multi-soliton solution for nonlinear waves in a stratified fluid of finite depth. *Phys. Lett. A* **74**, 233–235.

https://doi.org/10.1017/jfm.2025.10719 Published online by Cambridge University Press

McAllister, M.L., Draycott, S., Calvert, R., Davey, T., Dias, F. & van den Bremer, T.S. 2024 Three-dimensional wave breaking. *Nature* **633**, 601–607.

Michele, S. & Renzi, E. 2020 Effects of the sound speed vertical profile on the evolution of hydroacoustic waves. *J. Fluid Mech.* **883**, A28.

Naumkin, P.I. & Sánchez-Suárez, I. 2018 On the modified intermediate long-wave equation. *Nonlinearity* **31**, 980–1008.

Ono, H. 1975 Algebraic solitary waves in stratified fluids. *J. Phys. Soc. Japan* **39**, 1082–1091.

Ren, Y., Dong, H., Zhao, B. & Fu, L. 2023 Higher-order Benjamin–Ono model for ocean internal solitary waves and its related properties. *Axioms* **12**, 969.

Vishnu Priya, N., Thulasidharan, K. & Senthilvelan, M. 2025 Hybrid solutions of real and complex modified Korteveg–de Vries equations and their predictions through deep learning algorithm. *Nonlinear Dyn.* **113**, 13585–13613.

Vlasenko, V. & Stashchuk, N. 2015 Three-dimensional shoaling of large-amplitude internal waves. *J. Geophys. Res. Oceans* **120**, 7905–7924.

Xu, J.X., Chen, Z.W., Xie, J.S. & Cai, S.Q. 2016 On generation and evolution of seaward propagating internal solitary waves in the northwestern South China Sea. *Commun. Nonlinear Sci. Numer. Simul.* **32**, 122–136.

Yu, D., Fu, L. & Yang, H.W. 2021 A novel dynamic model and the oblique interaction for ocean internal solitary waves. *Nonlinear Dyn.* **108**, 491–504.

Yu, D. & Song, J.B. 2024 The modified cubic Benjamin–Ono equation describing internal solitary waves in the deep ocean and its related properties. *Phys. Fluids* **36**, 067107.

Zeidan, D., Pandey, M. & Govekar, S. 2022 Interaction of shock and discontinuity waves at the stellar surfaces. *Phys. Fluids* **34**, 066111.

Zheng, Q., Klemas, V. & Yan, X.H. 1997 Digital orthorectification of space shuttle coastal ocean photographs. *Intl J. Remote Sens.* **18**, 197–211.

Zhi, C.H., Fan, W.H. & You, Y.X. 2024 Assessment of unidirectional internal solitary wave models in a two-layer fluid system through an improved experimental method. *Ocean Engng* **312**, 119046.

https://doi.org/10.1017/jfm.2025.10719 Published online by Cambridge University Press